Amorphous Silicon Two-Color Microbolometer for Uncooled IR Detection

Mahmoud Almasri, *Member, IEEE*, Bai Xu, *Member, IEEE*, and James Castracane

***Abstract*—This paper describes the modeling and design of two-color microbolometers for uncooled infrared (IR) detection. The goal is to develop a high resolution IR detector array that can measure the actual temperature and color of an object based on two spectral wavelength regions. The microbolometer consists of high temperature amorphous silicon (a-Si:H) thin film layer held above the substrate by Si_3N_4 bridge. A thin NiCr absorber with sheet resistance of 377 Ω/sqr is used to enhance the optical absorption in the medium and long IR wavelength windows. A tunable micromachined Al-mirror was suspended underneath the detector. The mirror is switched between two positions by the application of an electrostatic voltage. The switching of the mirror between the two positions enables the creation of two wavelength response windows, 3–5 and 8–12 μm. A comparison of the two response wavelength windows enables the determination of the actual temperature of a viewed scene obtained by an IR camera. The microbolometer is designed with a low thermal mass of 1.65×10^{-9} J/K and a low thermal conductance of 2.94×10^{-7} W/K to maximize the responsivity R_v to a value as high as 5.91×10^4 W/K and detectivity D^* to a value as high as 2.34×10^9 cm Hz$^{1/2}$/W at 30 Hz. The corresponding thermal time constant is equal to 5.62 ms. Hence, these detectors could be used for 30-Hz frame rate applications. The extrapolated noise equivalent temperature difference is 2.34 mK for the 8–12 μm window and 23 mK for the 3–5 μm window. The calculated absorption coefficients in the medium and long IR wavelength windows before color mixing are 66.7% and 83.7%. However, when the color signals are summed at the output channel, the average achieved absorption was 75%.**

***Index Terms*—Amorphous silicon, microelectromechanical systems (MEMS), microbolometer, simulation, uncooled IR detection.**

I. Introduction

UNCOOLED IR cameras provide moderate performance at low cost to meet a broader range of civilian and military applications [1], [2]. The operation of the IR camera is restricted to 3–5 μm (medium IR wavelength) and 8–12 μm (long IR wavelength) portion of the electromagnetic spectrum due to the existence of windows in the atmosphere that allow transmission of radiation at these wavelengths. The IR camera generates pictures from the IR radiation naturally emitted from all objects. The generated image shows the surface temperature variations of target objects in a viewed scene with a "black-hot" fashion [3]. The current existing uncooled focal plane arrays (FPAs) are using either the medium or long wavelength windows to generate an image from a viewed scene. The achieved noise equivalent temperature difference (NETD) ranges between 20–100 mK and operates at 30-Hz frame rate which correspond to a time constant $<$10 ms [4], [5]. In this paper, a microbolometer is designed to operate near the background-limited noise performance with a NETD between 2.3–21 mk with a fill factor as high as 75%. The high-temperature resolution was achieved by the reduction in thermal conductance, which improved responsivity and detectivity of the microbolometers and, hence, improved the NETD. In addition, the microbolometer is designed with two colors by measuring the viewed scene response at both the medium and the long IR wavelength windows. The calculated thermal time constant is comparable to the commercially available FPAs, i.e., 10 ms. This work builds upon the design performed by Leonov and Butler by utilizing both the medium and long wavelength regions. In their design, the color microbolometer operation is restricted to the long wavelength region (8.0–10.5 and 10.5–14 μm) [6].

Manuscript received November 1, 2004; revised September 30, 2005. This work was supported by the New York State Office of Science, Technology, and Academic Research. The associate editor coordinating the review of this paper and approving it for publication was Dr. Usha Varshney.

M. Almasri is with the Department of Electrical and Computer Engineering, University of Missouri, Columbia, MO 65211 USA (e-mail: almasrim@missouri.edu).

B. Xu and J. Castracane are with the College of Nanoscale Science and Engineering, State University of New York at Albany, Albany, NY 12203 USA (e-mail: bxu@uamail.albany.edu; jcastrcane@uamail.albany.edu).

Digital Object Identifier 10.1109/JSEN.2006.870139

II. Background and Theory

A microbolometer is a thermal sensor whose resistance changes with temperature, associated with the absorption of IR radiation. Its performance is characterized by several figures of merits such as responsivity (R_v), temperature coefficient of resistance (TCR), detectivity (D^*), and NETD. NETD is a system figure of merit. It is defined as the temperature change at the target, which produces a signal in the microbolometer equal to the total noise (RMS) [7]–[9], [13], [14]. The total noise voltage (V_n) that exists in a microbolometer is given by the sum of squares of the contributions due to Johnson noise (ΔV_J), $1/f$ noise [10], temperature fluctuation noise (ΔV_{TF}), and background noise (ΔV_{BG}). Therefore, high sensitivity can be achieved by minimizing the total noise and maximizing the R_V, and D^* and have a large value of TCR.

The power that radiates from a target object in a viewed scene between $(\lambda_1 - \lambda_2)$ at $T_{\rm obj}$ with an emisivity of $\varepsilon(\lambda)$ is given by

$$M_{\rm obj}(\lambda, T_{\rm obj}) = \int_{\lambda_1}^{\lambda_2} M(\lambda, T_{\rm obj})\varepsilon(\lambda)d\lambda \qquad (1)$$

where λ is the wavelength, $T_{\rm obj}$ is the absolute temperature of a target object in a viewed scene, and $M(\lambda, T_{\rm obj})$ is the amount of power that leaves an object per unit area which is known as spectral exitance [7]. On the other hand, the detected power

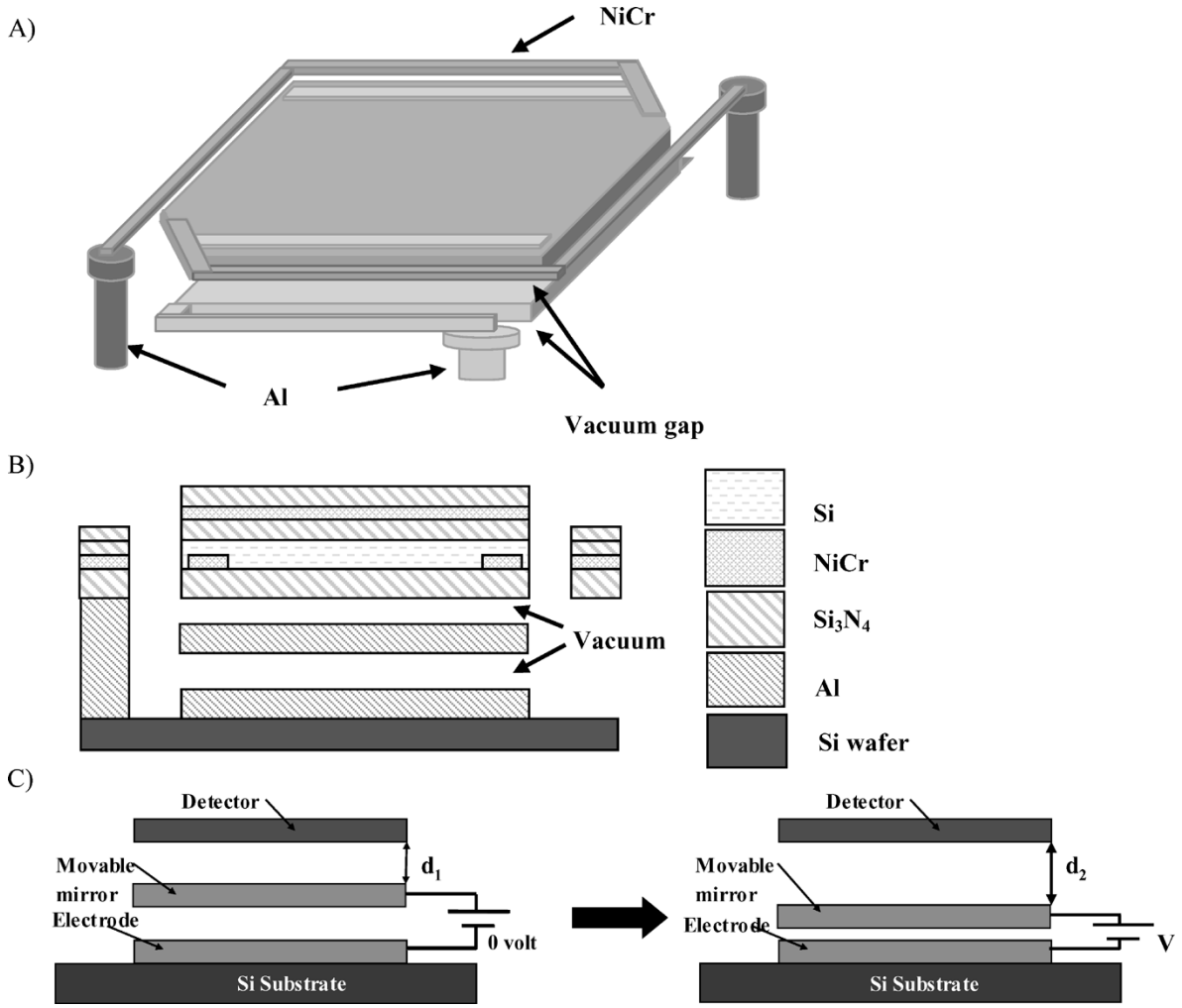

Fig. 1. Two-color microbolometer geometry: A) top view, B) side view, and C) operational view. The schematics show the device geometry consisting of movable Al-mirror, single NiCr absorber, Si_3N_4 membrane and passivation layer, and NiCr electrode arms and contacts to the suspended high TCR amorphous silicon. The air microcavity is located between the underlying Al mirror and the high TCR amorphous silicon. The movable micromirror creates a tunable resonant cavity between the detector and the mirror. The detector can be tuned to two spectral bands by changing the cavity depth by applying electrostatic voltage as indicated in the figure.

that absorbed by the detector is significantly less because the detector can collect the power within a limited solid angle

$$P_D(\lambda, T_{\rm obj}) = \frac{1}{4(F/\#)+1} \times \int_{\lambda_1}^{\lambda_2} M(\lambda, T_{\rm obj})\varepsilon(\lambda)\eta(\lambda)\varepsilon_a(\lambda)\varepsilon_o(\lambda)d\lambda \quad (2)$$

where $F/\#$ is the focal ratio of the objective, $\eta(\lambda)$ is the absorption of the detector $\tau_{\rm a}(\lambda)$, and $\tau_{\rm o}(\lambda)$ are the transmitivities of the atmosphere and objective, respectively. The transmitivities of the atmosphere and objectives are assumed to be unity. Changes of the detected optical power cause a change in the detector temperature and, hence, changes the detector response. The change of the detected power (P_D) per $\Delta T_{\rm obj}$ is determined by differentiating the previous equation

$$\frac{\Delta P_D}{\Delta T_{\rm obj}} = \frac{\tau_{atm}\tau_o\varepsilon(\lambda)\eta(\lambda)A}{4(F/\#)^2+1}\left(\frac{\Delta M}{\Delta T_{\rm obj}}\right)_{\lambda_1-\lambda_2}. \quad (3)$$

$(\Delta M/\Delta T_{\rm obj})_{\lambda_1-\lambda_2}$ is the temperature contrast, i.e., the change of IR power radiated by a blackbody object within the $(\lambda_1-\lambda_2)$ region when its temperature changes by $\Delta T_{\rm obj}$ [7], [8], [11]. The actual temperature of an object can be determined by calculating the ratio of the change of the detected power in two spectral regions.

III. Microbolometer Optical Design

The microbolometer is designed with a movable reflecting Al micromirror between the underlying silicon substrate and the suspended high TCR a-Si:H membrane. The position of the Al mirror is changed before each exposure to IR power to create two-resonant cavities between the mirror and the a-Si:H layer with a peak wavelength at 4.3 and 10 μm. A schematic of the two-color microbolometer along with the operational view is shown in Fig. 1. Two resonant cavities between the incoming and reflected waves can be created if the cavity-depth is tuned according to

$$d_n = \frac{[(2n-1)-(\varphi 2-\varphi 1)]\,\lambda}{4} \quad (4)$$

where d_n is the air gap depth, n is an integer, and φ_1 and φ_2 are the phase differences between the incoming and reflected light

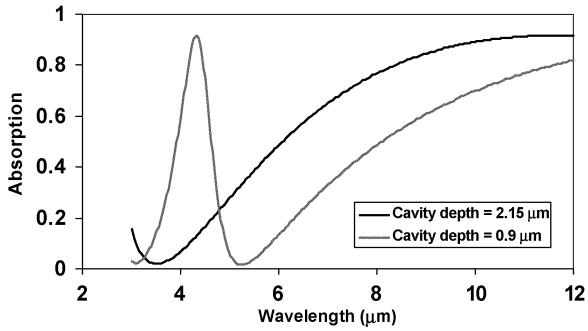

Fig. 2. Calculated absorption spectra versus wavelength for 0.9 and 2.15 μm cavity depths. A thin NiCr absorber was used to enhance the absorption at medium and long wavelength.

[8], [12]. The resonant cavity depth is optimized to maximize the absorption and, hence, increase the responsivity of the microbolometer between 3–5 and 8–12 μm windows. The two-band design is used to create a two-color microbolometer to obtain high-resolution image. A transmission line model was used to match the impedance of the thicknesses of the microbolometer layers; Si_3N_4 bridge, a-Si:H heat sensitive material layer, NiCr absorber, and the air gap height to free space impedance 377 Ω [13], [14]. The result was an enhanced absorption with an absorption value of 89.1% and 69.8% for cavity depth of 0.9 and 2.15 μm, respectively. In the first case, the absorption was maximized in the long wavelength window while in the second case the absorption was maximized in the medium wavelength window. The absorption was plotted as a function of wavelength for both cavity depths as shown in Fig. 2.

The thermal mass of the microbolometer was calculated from the specific heat capacity and volume of each layer forming the microbridge, namely a-Si membrane, the Si_3N_4 support and passivation layers, NiCr absorber, NiCr-contacts, and 1/3 of each NiCr-electrode arms. The thermal mass is given by

$$C = \sum_n W_n L_n t_n c_n + \frac{2}{3} \sum_m W_m L_m t_m c_m \tag{5}$$

where W_n, L_n, and t_n correspond to width, length, thickness, and specific heat of each thin film layer, and W_m, L_m, t_m, and c_m correspond to width, length, thickness, and specific heat of each layer of the electrode arms.

Finite element analysis using ANSYS and Intellisuite tools have been employed to provide accurate prediction of the microbolometer and micromirror performance. The simulations were performed using published material properties of all thin film layers. In this model, an input text file is used where the design parameters can be easily changed. The resulted deflection and stress distribution (Von Mises) of the electrode arms and the pixel due to the internal forces that acted on the microbolometer, which includes the axial force, shear, moment and torque were calculated and plotted in Fig. 3. In addition, the micromirror moves by applying electrostatic voltage between its surface and the bottom electrode. In static equilibrium, the micromirror is stable since the mechanical torque and the electrostatic torque are equalized. As the voltage is increased slightly above a certain voltage, the electrostatic torque overcomes the mechanical torque, and, hence, the mirror becomes unstable and pulls-down rapidly until it touches the bottom electrode. In order to prevent this pull-in behavior, the mirror movement should be between one-third and one-half of the air gap depth [15]. The Al mirror was displaced 1 μm by applying 14 V. In general, the result shows that the microbolometer and the Al-micromirror have flat surfaces and low stress distribution. The deflection of the electrode arms and the pixel was less than 1%.

The optical radiation falling on the detectors goes into heating the pixel. Hence, heat flows from the pixel to the surrounding via three heat-transfer mechanisms, conduction, convection, and radiation. The conduction mechanism occurs through the electrode arms and the surrounding air. Therefore, the electrode arms must be carefully designed to reduce the thermal conductance path and to meet the thermal time response requirements The IR sensitive element must be thermally isolated from its surroundings to reduce the rate of heat loss and, hence, increase the sensitivity of the detector. Therefore, the pixel arrays must be packaged in vacuum. The convection mechanism occurs in the presence of a surrounding atmosphere. If the principal heat loss mechanism is radiative, then the detector is at the background limit. In this design, the detector will be packaged in vacuum. Therefore, the thermal conductance of the microbolometers is mainly due to the heat flow via the supporting arms. The thermal conductance was estimated from the calculated thickness, width and length of the electrode arms simulated in the electromechanical model. Since the thermal conductance of the individual components making up the electrode arms were in parallel, the total thermal conductance $G_{\rm tot}$ was determined by the summation of the individual thermal conductance of all layers, namely: the Si_3N_4 support layers, NiCr electrical conductive layer, and high TCR a-Si:H layer. The total thermal conductance is given by

$$G_{\rm tot} = \sum_m \frac{K_m W_m t_m}{L_m} \tag{6}$$

where K_m is the thermal conductivity of each component, and W_m, L_m, and t_m correspond to width, length, and thickness of each component. The thermal time constant τ_{th} was calculated from the ratio of the device's thermal mass to its thermal conductance C/G. A low thermal time constant was targeted for high-speed camera applications.

IV. Microbolometer Structure

The microbolometer thin film layers were carefully selected. A 4.5-nm-thick layer of NiCr was chosen as an absorber material with a sheet resistance of 377 Ω/sqr. The NiCr absorber was employed to enhance the absorption at the medium and long wavelength windows. Several other metals such as Ti could be used as an absorber [13]. A layer of amorphous silicon with a thickness of 130 nm was selected as the temperature sensitive material. A-Si:H has low noise properties, high TCR, and can be prepared with a range of electrical resistivities to meet sensor resistance specifications [12], [16]–[18]. Several other IR sensitive material can be used instead such as vanadium oxide, VO_x with a TCR of 2%/K [19], [20], Polycrystalline-silicon, Poly-Si with a TCR of 1–2%/K [21], semiconducting Y-Ba-Cu-O with a TCR of 3.1%/K [22], [23], Polycrystalline silicon germanium

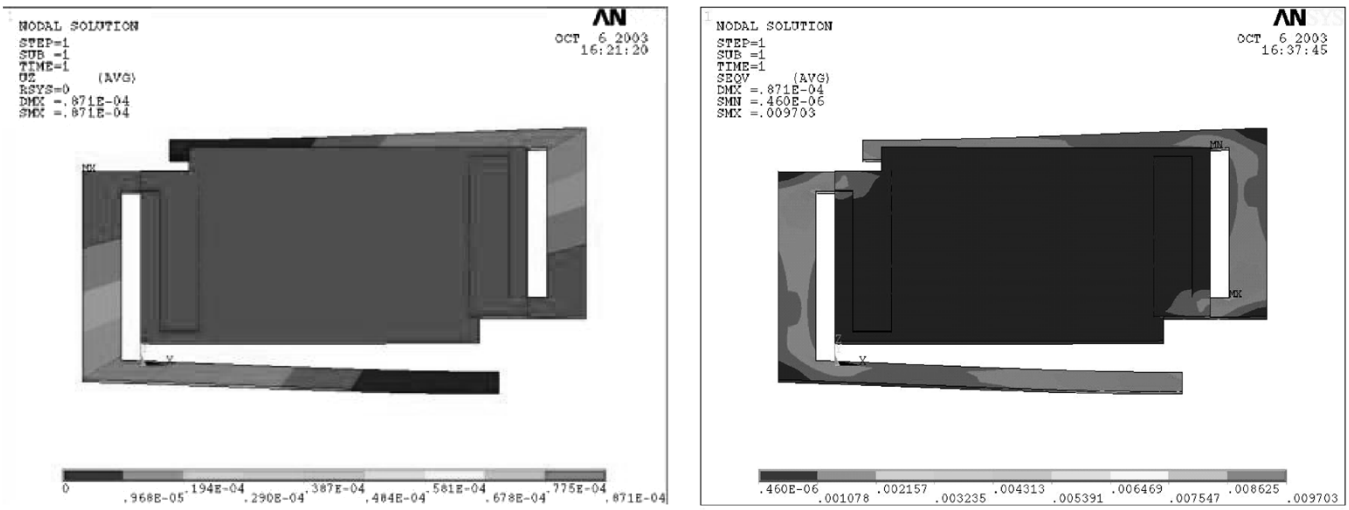

(a) (b)

Fig. 3. Three-dimensional view of finite element simulation of the microbolometer. (a) The plot shows an optimized microbolometer structure with slight deflection less than 1% of the air gap height. (b) Von Mises stress distribution shows the microbolometer with flat surface.

alloy, Poly-Si-Ge with a TCR of 0.75–2%/K [24], [25], and thin metal films such as titanium with TCR of 0.2%–0.25% at 300 K [26], [27]. Next, a 170-nm-thick Si_3N_4 bridge was suspended above the underlying Si substrate. The Si_3N_4 was chosen because of its excellent thermal and mechanical material properties and excellent processing characteristics. The Si_3N_4 has two absorption peaks, the first at 3.4 μm and the second at 11.5 μm [28]. A second layer of Si_3N_4 with a thickness 50 nm was used to prevent electrical contact between the a-Si:H and the NiCr absorber. A third layer of Si_3N_4 with a thickness of 40 nm was used to passivate the NiCr absorber from oxidation during the removal of the polyimide sacrificial layer to release the microbolometer. Next, NiCr was used as the contact and electrode material because it makes the best contact to a-Si:H resulting in linear behavior and because it has a relatively low thermal conductivity, therefore, provides a better thermal isolation. Next vacuum cavities with depths of 0.9 and 2.15 μm are used to create the $\lambda/4$ wavelength resonant-cavities at two separate windows, and provide thermal isolation from the underlying substrate. A movable Al mirror with a thickness of 300 nm was chosen to reflect the IR radiation back to the detector and to enable the creation of two resonant cavities. Finally, a silicon substrate with a resistivity of 10 Ω cm is used. A complete list of the calculated film thickness and their electrical and thermal properties are shown in Table I.

The color microbolometer design realization can be achieved by assuming the following fabrication sequence. Initially the wafer was thermally oxidized to grow a thick SiO_2 for insulation. Next, a seed layer consisting of chromium (Cr), gold (Au), and titanium (Ti) thin films were sputtered deposited. The Ti was etched to form the bottom electrode which also serves as a reflective mirror. The wafer was then coated with a photoresist sacrificial layer and patterned to form a mold. Au was electroplated inside the mold and created the mirror anchors. Next, the photoresist was removed with acetone and the Cr/Au seed layers were wet etched. The wafer was then spin coated with polyimide sacrificial layer and cured at 300 °C. The polyimide was then polished to clear the anchors. An Al layer was sputtered and patterned to form the top mirror and torsion beams. The model predicted that the mirror will have a smooth and flat surface during actuation. However, keeping the mirror flatness is another challenge. Other materials such as low stress electroplated nickel can be used [29]. Next, photoresist was spin coated and pattern to create mold for the electroplating the anchors of the microbolometer. Au was electroplated inside the mold. Again, the photoresist layer was removed with acetone. The second sacrificial layer was spin coated and cured at lower temperature (270 °C) and polished to clear the Au anchors. A thick Si_3N_4 membrane material was deposited by PECVD. The metallization layer consisting of NiCr electrode arms and contacts/pads was (V_n) that exists in a microbolometer deposited and patterned. Next, a Si:H thermometer layer was subsequently sputter deposited. The a Si:H pixel was patterned and dry etched. A thin layer of Si_3N_4 was deposited PECVD followed by sputtering of a thin NiCr absorber. The absorber was patterned. A Si_3N_4 passivation layer was deposited. Next, All Si_3N_4 layers were pat-

TABLE I
MICROBOLOMETER A) LAYERS THICKNESS AND B) PROPERTIES THAT WERE USED IN MODELS. THE MICROBOLOMETER ELECTRODE ARM LENGTH IS $87 \times 4\ \mu m^2$

A)

Layers	Thickness (nm)	Pixel Area (μm)	Arms Thickness (nm)
Si_3N_4 passivation	40	40×40	40
NiCr Absorber	5	40×40	-
Si_3N_4 Insulator	50	40×40	50
a-Si (High TCR)	130	40×40	-
NiCr arms	50	40×40	50
NiCr contacts	50	3×36	-
Si_3N_4 Membrane	170	40×40	170
Al movable mirror	250	40×40	250
Si-wafer	-	-	-

B)

Layers	Thickness (nm)	Thermal Conductivity G (W/K)	Thermal mass C (Joule/K)	Permitivity	Resistivities (Ω m)
Si_3N_4	40	0.10	2.8	4	1×10^{13}
NiCr	5	0.12	0.843	30	110×10^{-8}
a-Si	130	0.745	1.64	11.8	5×10^{-4}
Al mirror	250	1.32	2.42	1	2.6×10^{-8}

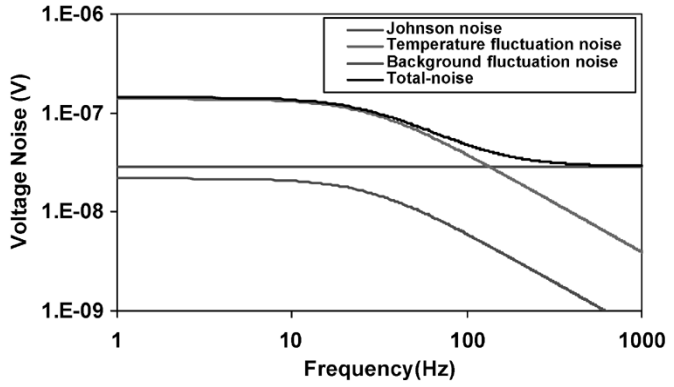

Fig. 4.Johnson voltage noise, temperature fluctuation voltage noise, background fluctuation noise, and total voltage noise were calculated as a function of chopper frequency.

terned and dry etched to expose the polyimide to oxygen ashing in the final step. Finally, the polyimide sacrificial layers were removed by oxygen plasma. At this stage, the microbolometer is ready for characterization.

V. Microbolometer Performance

In the model, the microbolometer has a resistance value equals to 50 KΩ and TCR equals to 2.7%/K [12]. The microbolometer was dc biased with a bias current up to 25 μA which correspond to a voltage bias of 0.75 V across the microbolometer. The microbolometer exhibited low noise voltage and operated near background limited noise voltage. The Johnson voltage noise, the temperature fluctuation voltage noise, the background fluctuation noise, and the total voltage noise were calculated as a function of chopper frequency and plotted in Fig. 4. The 1/f noise was not accounted for in the calculation of the total noise because the detector will be biased in the Johnson noise level region and the 1/f noise depends on many process technology factors related to the microbolometer fabrication. Therefore, the 1/f noise does not affect the capabilities of the proposed design. The responsivity and detectivity were calculated for the 3–5 μm and the 8–12 μm IR transparency windows. The calculated responsivity and detectivity were plotted versus chopper frequency in Fig. 5. The responsivity was maximized by enhancing the absorption in these two windows and by achieving low thermal mass and low thermal conductance of the detector. The calculated thermal mass and thermal conductance were 1.65×10^{-9} (J/K) and 2.94×10^{-7} W/K, respectively. However, the thermal conductance through the electrode arms should not be made as small as possible without consideration of response time requirement. Therefore, the thermal capacity should be made as small as possible until the thermal response time becomes close to the 60-Hz frame rate. It should be pointed out that the support legs serve as support structures, conductive legs and thermal isolation legs. In addition, the high values of responsivity and detectivity will allow for improved NETD to a value as low as 2.43 and 23 mK for an 8–12 and 3–5 μm window, respectively. The NETD is plotted versus chopper frequency in Fig. 5. A complete list of the microbolometer performance results is shown in Table II.

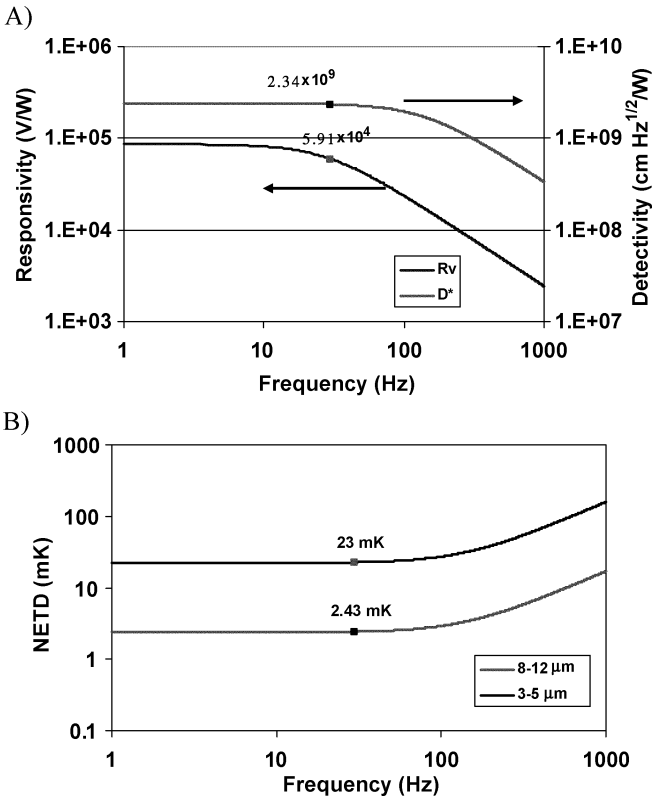

Fig. 5. A) Responsivity and detectivity and B) NETD as a function of chopper frequency at different current bias values measured in vacuum with a 0.6–15 μm broadband IR radiation at 1470 K.

TABLE II
Two-Color Microbolometer Performance Characteristics at 30 Hz

Thermal time constant (ms)	**5.62**
Fill Factor %	**73**
Absorption	**0.75**
TCR (%/K)	**2.7**
Thermal capacity (J/K)	**1.65×10^{-9}**
Thermal conductance (W/K)	**2.94×10^{-7}**
Johnson Noise (V)	**2.87×10^{-8}**
Temperature Fluctuation Noise (V)	**9.52×10^{-8}**
Background Noise (V)	**1.49×10^{-9}**
Responsivity (V/W)	**5.91×10^{4}**
Detectivity (cm Hz$^{1/2}$/W)	**2.34×10^{9}**
Calculated NETD (mK)	**2.43 between 8-12 μm 23 between 3-5 μm**

VI. Results and Discussion

The spectral exitance $\mathrm{M}(\lambda)$ of a target object corresponds to that of a blackbody source multiplied by its emissivity $\varepsilon(\lambda)$ at the viewed scene temperature. Therefore, information on emissivity is important for an accurate estimate of temperature of the viewed scene. However, determination of emissivity is tedious work; therefore, the spectral exitance of an object is determined from the detected power calculations. The spectral exitance of a blackbody was not discussed in this paper; further details can be found in [7]. The detected radiated power of a target object was significantly less than the radiated one and is dependent on the optical absorption of the detector. Since the vacuum gap is changing between two depths, the optical absorption and, hence, the detected power were maximized with an absorption

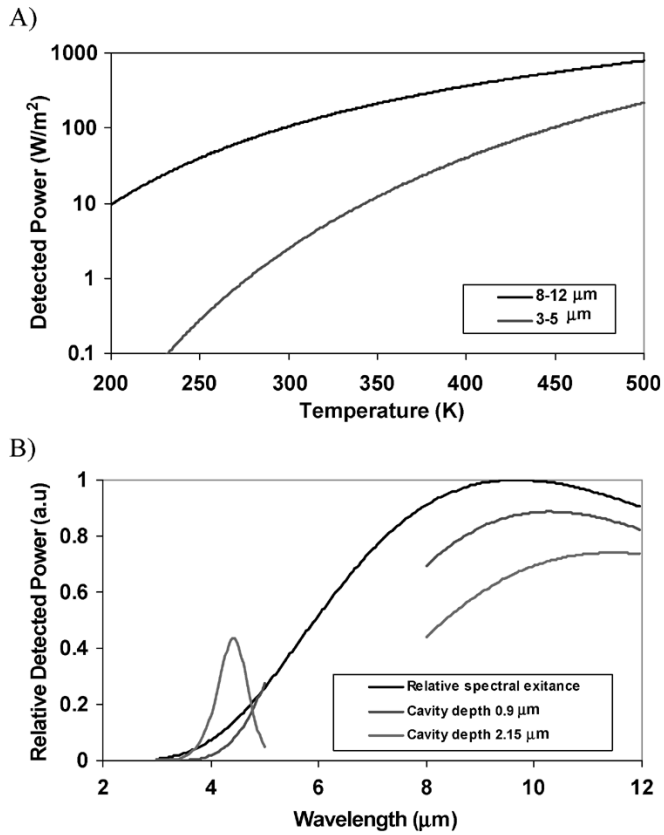

Fig. 6. Detected power is A) plotted as a function of temperature and B) normalized relative to the maximum spectral exitance of a viewed scene and plotted as a function of wavelength.

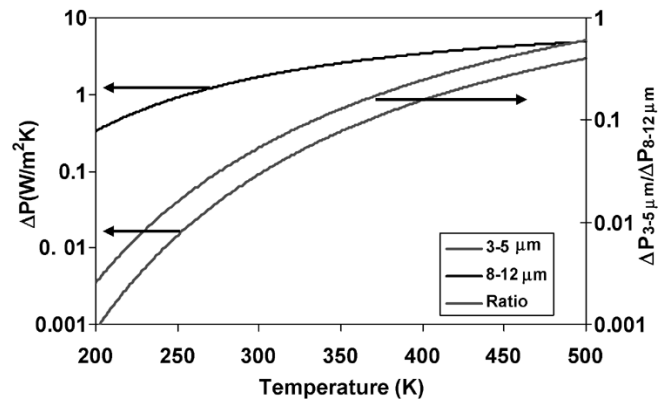

Fig. 7. Temperature contrast $(\Delta P/\Delta T)_{3-5\ \mu m}$ and $(\Delta P/\Delta T)_{8-12\ \mu m}$ and the ratio $\Delta P_{3-5}/\Delta P_{8-12}$ of a viewed scene are plotted as a function of temperature.

peak in the 3–5 and 8–12 μm windows when the cavity depth is 2.15 and 0.9 μm, respectively. The detected power was calculated relative to the total radiated power at the medium and long wavelength of a viewed scene. The results at 300 K were 0.43, and 0.87, respectively. It is important to note that the detected power changes slightly with a change of temperature of the viewed scene. The detected power is plotted as a function of temperature Fig. 6, and is normalized relative to the maximum spectral exitance of a viewed scene and plotted as a function of wavelength in the same figure. The change of the detected power

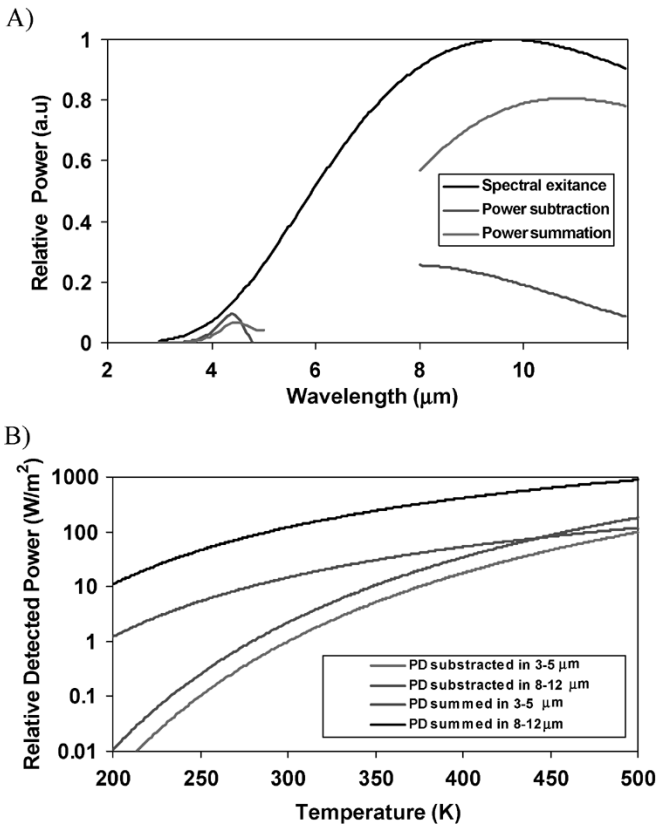

Fig. 8. Total received powers at the output channel for 3–5 and 8–12 μm windows and for both cavity depths as the power subtracted or summed at the output channel as a function of A) wavelength and B) temperature.

(ΔP_D), absorbed by the detector was calculated as a function of temperature for the same two spectral windows. The absorbed power (P_D), the change of the detected power (ΔP_{3-5}) and ΔP_{8-12}, and the ratio of $\Delta P_{3-5}/\Delta P_{8-12}$, plays an important role; they determine the sensitivity of the IR camera and determine the actual temperature of a viewed scene. The change in detected power, ΔP_{3-5} and ΔP_{8-12}, as well as the ratio $\Delta P_{3-5}/\Delta P_{8-12}$ of a viewed scene are plotted as a function of temperature in Fig. 7.

The output signal of the microbolometer at both cavity depths can be summed or subtracted at either the readout electronic level or the output level. In the first case, an offset value is required because the output signals for both colors are changing with temperature. At 300 K an offset of 0.43 V_{signal} is required and at 500 K an offset of 0.40 V_{signal} is required. The slight difference of the offset does not seem to affect the measurement of the actual temperature of the viewed scene.

In the second case, the total received powers at 3–5 and 8–12 μm windows for both cavity depths are summed (averaged) at the output channel. The summation of the signals resulted in total absorption (for one frame period) of 75.3%. In addition, the signals can be subtracted at the output channel. In this case, the power received in the 3–5-μm output channel is equal to the power received at 0.9-μm cavity depth subtracted from the power received at 2.15-μm cavity depth. Similarly, the power received in the 8–12-μm output channel is equal to the power received at 2.15-μm cavity depth subtracted from the power received at 0.9-μm cavity depth. The results of total received

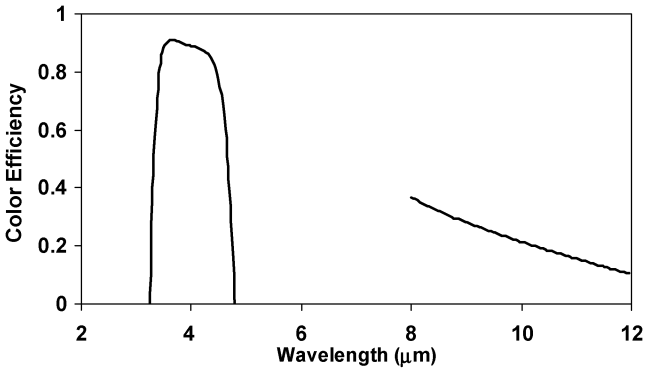

Fig. 9. Efficiencies of the two-color signals at the output channel for both medium and long wavelength spectral windows at room temperature are plotted as a function of wavelength. In this case, the responses are subtracted.

power relative to maximum exitance due to summation and subtraction of power at the output channel along with the relative spectral exitance of a viewed scene are plotted as a function of wavelength and temperature in Fig. 8, respectively. The optical absorption for both cavity depth of 2.15 and 0.90 μm were calculated from the received power in the two spectral windows divided by the total spectral radiance in the same two windows of a viewed scene. The calculated absorption at room temperature was 83.7% and 66.9%, respectively. The absorption showed constant value as the temperature changing from 200–500 K.

In this model, the 3–5 and 8–12 μm spectral windows are corresponding to the two-colors are detected by the microbolometer. The efficiencies of the two-color signals at the output channel for both medium and long wavelength spectral windows at room temperature are equal to 62.4% in comparison to 78.8% before color mixing and 21.8% compared to 11.1% before color mixing, respectively. The results are plotted as a function of wavelength in Fig. 9. In addition, it is found that the efficiency changes very slightly with temperature from 200–500 K.

VII. Conclusion

A two-color microbolometer is designed. The color microbolometer is based on a tunable micromirror fabricated underneath the detector. The micromirror moves between two positions to create two resonant vacuum cavities. The cavity depths maximize the optical absorption between 3–5 μm and 8–12 μm window to create the two-color image of a viewed scene. The maximum achieved optical absorption's were 89.1% and 69.8% for cavity depth of 0.9 and 2.15 μm, respectively. The ratio of the change of spectral exitance and the ratio of change of the absorbed power in the two spectral windows are used to make an accurate estimate of the actual temperature of a viewed scene. The designed microbolometer exhibited high performance. The achieved responsivity was 5.91×10^4 V/W and the detectivity was above 10^9 cm $\mathrm{Hz}^{1/2}/\mathrm{W}$. In addition, the microbolometer operates near background-limited noise with NETD between 2.43–23 mK. The calculated thermal time constant was 5.62 ms for each color. Hence, these detectors could be used for 30 Hz frame rate applications. An offset of 40%–43% at the readout electronics is necessary to allow total color separation. The slight difference of the offset does not seem to affect the measurement of the actual temperature of a viewed scene. The color efficiencies of the two signals at the output channel for medium and long IR wavelength spectral windows at 300 K are 62.4% and 21.8%, respectively.

References

[1] T. Breen, M. Kohin, C. A. Marshall, R. Murphy, T. White, A. L. Leary, and T. Parker, "Even more applications of uncooled microbolometer sensors," *Proc. SPIE*, vol. 3698, pp. 308–318, 1999.

[2] T. Breen, N. Butler, M. Kohin, C. A. Marshall, R. Murphy, T. Parker, N. Piscitelli, and R. Silva, "A summary of applications of uncooled microbolometer sensors," in *Proc. IEEE Aerosp. Conf.*, vol. 3, 1999, pp. 361–374.

[3] R. A. Wood and N. A. Foss, "Micromachined bolometer arrays achieve low-cost imaging," *Laser Focus World*, pp. 101–106, Jun. 1993.

[4] "*Proc. SPIE*,", 1998.

[5] R. Murphy, M. Kohin, B. Backer, N. Butler, R. Blackwell, and T. Allen, "Recent development in uncooled IR technology," *Proc. SPIE*, vol. 4028, pp. 12–16, 2000.

[6] V. Leonov and D. Butler, "Two-color thermal detector with thermal chopping for infrared focal-plane arrays," *Appl. Opt.*, vol. 40, no. 16, pp. 2601–2610, 2001.

[7] E. L. Dereniak and G. D. Boreman, *Infrared Detectors and Systems*. New York: Wiley, 1996.

[8] P. W. Kruse and D. D. Skatrud, "Uncooled Infrared Imaging Arrays and Systems," in *Semiconductors and Semimetals*. New York: Academic, 1997, vol. 47, pp. 17–42.

[9] P. W. Kruse, "The design of uncooled infrared imaging arrays," *Proc. SPIE*, vol. 2746, pp. 34–37, 1994.

[10] F. N. Hooge, "1/f noise is no surface effect," *Phys. Lett.*, to be published.

[11] V. Leonov and D. Butler, "Two-color thermal detector with thermal chopping for infrared focal-plane arrays," *Appl. Opt.*, vol. 40, no. 16, pp. 2601–2610, 2001.

[12] T. Schimert, D. Ratcliff, J. Brady, S. Ropson, R. Gooch, B. Ritchey, P. McCardel, K. Rachels, M. Wand, M. Weinstein, and J. Wynn, "Low cost, low power uncooled a:Si based micro infrared camera for unattended ground sensor applications," *Proc. SPIE*, vol. 3713, pp. 101–111, 1999.

[13] M. Almasri, Z. Çelik-Butler, D. P. Butler, A. Yaradanakul, and A. Yildiz, "Uncooled multimirrors broad-band infrared microbolometers," *J. Microelectromech. Syst.*, vol. 11, no. 5, Oct. 2002.

[14] ——, "YBaCuO microbolometers for broad-band IR sensing," *Proc. SPIE*, pp. 264–273, Apr. 2001.

[15] O. Degani, E. Socher, A. Lipson, T. Leitner, D. J. Setter, S. Kaldor, and Y. Nemirovsky, "Pull-in study of an electrostatic torsion microactuator," *J. Microelectromech. Syst.*, vol. 7, p. 373, 1998.

[16] C. Vedel, J. L. Martin, J. L. Ouvrier Buffet, J. L. Tissot, M. Vilain, and J. J. Yon, "Amorphous Silicon Based Uncooled Microbolometer IRFPA," *Proc. SPIE*, vol. 3698, pp. 276–283, 1999.

[17] K. C. Liddiard, U. Ringh, C. Jansson, and O. Reinhold, "Progress of swiedish-Australian research collaboration on uncooled smart Ir sensors," *Proc. SPIE*, vol. 3436, pp. 578–584, 1998.

[18] E. Mottin, J. L. Martin, J. L. Ouvrier Buffet, M. Vilain, and J. J. Yon, "320 × 240 microbolometer uncooled IRFPA," *Proc. SPIE*, vol. 4028, pp. 40–46, 2000.

[19] W. Radford, D. Murphy, M. Ray, S. Propst, A. Kennedy, J. Kojiro, J. Woolaway, K. Soch, R. Coda, G. Lung, E. Moody, D. Gleichman, and S. Baur, "320 × 240 silicon microbolometer uncooled IRFPA's with on-chip offset correction," *Proc. SPIE*, vol. 2746, pp. 82–93, 1996.

[20] B. E. Cole, R. E. Higashi, and R. A. Wood, "Monolithic arrays of micromachined pixels for infrared application," in *IEDM Tech. Dig.*, 1998, pp. 459–462.

[21] M. S. Liu, J. S. Haviland, and C. J. Yue, "Integrated infrared sensitive bolometers," U.S. Patent 005 260 225A, 1992.

[22] M. Almasri, D. P. Butler, and Z. Çelik-Butler, "Semiconducting YBCO bolometers for uncooled IR detection," in *Proc. SPIE*, vol. 4028, Apr. 2000, pp. 17–26.

[23] J. Gray, Z. Çelik-Butler, D. P. Butler, and M. Almasri, "Semiconducting YBaCuO infrared detecting bolometers," *Proc. SPIE*, vol. 3436, pp. 555–565, Jul. 1998.

[24] J. Wauters, "Doped silicon creates new bolometer material," *Laser Focus World*, pp. 145–149, 1997.

[25] V. Leonov, N. A. Perova, J. Vermeiren, B. Grietens, and C. Goessens, "Optimization of design and technology for uncooled poly-SiGe microbolometer arrays," *Proc. SPIE*, vol. 4721, pp. 122–133, 2002.

[26] A. Tanaka, S. Matsumoto, N. Tsukamoto, and N. Teranishi, "Silicon IC process compatible bolometer infrared focal plane array," presented at the 8th Int. Conf. Solid-State Sensors and Actuators, and Eurosensors IX, Stockholm, Sweden, Jun. 25–29, 1995.
[27] M. V. S. Ramakrishna, G. Karunasiri, U. Sridhar, and G. Chen, "Performance of titanium and amorphous Germanium microbolometer infrared detectors," *Proc. SPIE*, vol. 3666, pp. 415–420, 1999.
[28] P. Eriksson, J. Y. Andersson, and G. Stemme, "Thermal characterization of surface-micromachined silicon nitride membranes for thermal infrared detectors," *J. Microelectromech. Syst.*, vol. 6, pp. 55–61, 1997.
[29] M. Almasri and B. Frazier, "Micromirror arrays for high temperature operation," presented at the MRS Meeting, San Francisco, CA, Mar. 2005.

Mahmoud Almasri (S'01–M'03) received the B.Sc. and M.Sc. degrees in physics from Bogazici University, Istanbul, Turkey, in 1995 and 1997, respectively, and the Ph.D. degree in electrical engineering from Southern Methodist University (SMU), Dallas, TX, in 2001.

He is currently an Assistant Professor with the Department of Electrical and Computer Engineering, University of Missouri, Columbia. From 2001 to 2002, he was with General Monitors, Lake Forest, CA, as a Research Scientist. Previously, from 2002 to 2003, he was with Albany NanoTech as a Postdoctoral Research Associate; from 2004 to 2005, he was with the Georgia Institute of Technology, Atlanta, first as a Postdoctoral Fellow and then promoted to a Research Scientist position. His research interests are in the areas of MEMS, biomedical microsystems, integrated bio-detection systems, uncooled infrared microbolometers, microactuators, and micromirrors. He has coauthored more than 15 conference and journal papers in these areas.

Dr. Almasri is Member of SPIE. He was awarded the SMU Frederick E. Terman Award in electrical engineering (1999 to 2000) and the SMU Graduate Student Research Award in 2001.

Bai Xu (M'01) received the Ph.D. degree in material sciences from the National Scientific Research Center, France, in 1991.

He is an Assistant Professor with the College of Nanoscale Science and Engineering, State University of New York at Albany, and a Senior Scientist at Albany NanoTech. He has been involved in leading-edge research for more than 15 years and has hands-on experience in the area of nanotechnology, MEMS, and material sciences. His current research areas include nanotechnology, MEMS process development, device packaging, bioMEMS, and MEMS/IC integration.

James Castracane received the B.S. degree in physics from Canisius College, Buffalo, NY, in 1976, and the Ph.D. degree in physics from The Johns Hopkins University, Baltimore, MD, in 1981.

He is the Director of Technology at Albany NanoTech, Albany, NY, Associate VP/Professor at the College of Nanoscale Science and Engineering, State University of New York at Albany, and Director of the New York State Center for Advanced Technology in Nanomaterials and Nanoelectronics). In his current position, he directs the efforts of the faculty and research staff in areas which encompass materials science, optoelectronics, microsystems, and emerging fields such as molecular electronics and spintronics. His publication record spans over 100 articles, numerous invited or keynote presentations, and ten patents issued/pending.